





# The Induced Global Looping Magnetic Field on Mars

Lihui Chai<sup>1,2</sup> , Weixing Wan<sup>1</sup>, Yong Wei<sup>1</sup>, Tielong Zhang<sup>3</sup>, Willi Exner<sup>4</sup>, Markus Fraenz<sup>5</sup>, Eduard Dubinin<sup>5</sup>, Moritz Feyerabend<sup>4</sup>, Uwe Motschmann<sup>4,6</sup>, Yingjuan Ma<sup>7</sup>, J. S. Halekas<sup>8</sup>, Yi Li<sup>9</sup>, Zhaojin Rong<sup>1</sup>, and Jun Zhong<sup>1</sup> 

<sup>1</sup>Key Laboratory of Earth and Planetary Physics, Institute of Geology and Geophysics, Chinese Academy of Sciences, Beijing, People's Republic of China; [chailihui@mail.iggcas.ac.cn](mailto:chailihui@mail.iggcas.ac.cn)

<sup>2</sup>College of Earth and Planetary Sciences, University of Chinese Academy of Sciences, Beijing, People's Republic of China

<sup>3</sup>Space Research Institute, Austrian Academy of Sciences, Graz, Austria

<sup>4</sup>Institute for Theoretical Physics, TU Braunschweig, Braunschweig, Germany

<sup>5</sup>Max Planck Institute for Solar System Research, Goettingen, Germany

<sup>6</sup>DLR Institute of Planetary Research, Berlin, Germany

<sup>7</sup>Institute of Geophysics and Planetary Physics, University of California, Los Angeles, Los Angeles, CA, USA

<sup>8</sup>Department of Physics and Astronomy, University of Iowa, Iowa City, IA, USA

<sup>9</sup>University of Science and Technology of China, Hefei, People's Republic of China

Received 2018 December 18; revised 2019 January 17; accepted 2019 January 17; published 2019 January 28

## Abstract

Magnetic fields inconsistent with draped interplanetary magnetic fields and crustal fields have been observed on Mars. Considering the discovery of a global looping magnetic field around the Venusian magnetotail and the similarities in the solar wind interactions between Mars and Venus, we use Mars Atmosphere and Volatile Evolution observations to investigate the global looping field on Mars and its formation mechanism. It is found that a global looping field also exists on Mars; therefore, this type of global looping field is a common feature of unmagnetized planetary bodies with ionospheres, and therefore should also exist on Titan and near-Sun comets. The comparison of the looping fields on Mars and Venus shows that the looping field is stronger on Mars. Solar wind azimuthal flows around the magnetotail toward the  $-E$  magnetotail polar region ( $X_{MSE} < 0$ ,  $Y_{MSE} = 0$ ,  $Z_{MSE} < -1R_M$ ) are observed. We illustrate that the looping field can be formed by bending the draped field lines with these azimuthal flows, and that these azimuthal flows are associated with heavy ion plumes along the  $+E$  direction that are expected to be stronger on Mars than Venus. The current system associated with the looping field and its possible connection with the nightside ionosphere formations and ion escapes on Mars and Venus are discussed.

*Key words:* magnetic fields – planets and satellites: magnetic fields – plasmas – solar–terrestrial relations – solar wind

## 1. Introduction

The Martian magnetic environment has long been the subject of exploration and research. The upper limit of the Martian magnetic dipole moment has continued to narrow as missions more closely approached the planet (Dolginov 1987; Riedler et al. 1989; Mohlmann 1992; Acuna et al. 1998). Phobos-2 observed that the Martian magnetotail is mainly an induced structure composed of draped interplanetary magnetic fields (IMFs; Riedler et al. 1989; Yeroshenko et al. 1990). This observation shows that the solar wind interaction with Mars is similar to that with Venus, which is an interaction between solar wind and the planetary ionosphere and upper atmosphere (e.g., Saunders & Russell 1986). The Mars Global Surveyor (MGS) observed strong crustal magnetic fields on Mars (Acuna et al. 1998, 1999; Connerney et al. 1999) and showed that the crustal field influence on the global magnetic field extended to an altitude of 1300–1400 km (Brain et al. 2003). The initial observations of the newly launched Mars Atmosphere and Volatile Evolution (MAVEN) mission (Jakosky et al. 2015) show that the Martian crustal field may be responsible for twisting the magnetotail configuration (DiBraccio 2018). It also shows that the solar wind interaction with Mars is in some way similar to that with the Moon, which is an interaction between solar wind and the satellite's crustal magnetic field and surface (Luhmann et al. 2015). However, there are still large-scale magnetic fields that are inconsistent with both draped IMFs and crustal fields on Mars (Acuna et al. 1998; Dubinin et al. 2014a).

Based on statistical analysis of the initial MAVEN observations, Harada et al. (2015a) found that some of the magnetic fields in the  $-E$  hemisphere of the magnetotail are antiparallel to the IIMF, similar to what Zhang et al. (2010) found on Venus, where  $E$  is the solar wind conventional electric field. Based on statistical analysis of the MGS observations, Chai et al. (2016) suggested that there may be a global looping magnetic field around the magnetotail on Mars, similar to what they found on Venus. The large data gap in the MGS observations in the magnetotail region has lowered the confidence level of this result. In this Letter, we examine these abnormal magnetic fields using the MAVEN data.

The  $E$ -asymmetry structure and looping structure of the abnormal magnetic fields were first studied on Venus (Vaisberg & Smirnov 1980; Verigin et al. 1993; Zhang et al. 2010; Chai et al. 2016). Due to the lack of strong dipole and crustal fields (Russell et al. 1979), the abnormal magnetic fields inconsistent with draped IMFs on Venus are very easy to spot and have received substantial attention (Saunders & Russell 1986; Zhang et al. 2010; Dubinin et al. 2014b). By statistically analyzing the Venus Express (VEX) magnetic field observations, Zhang et al. (2010) found the  $E$ -asymmetry structure in the near magnetotail that the draped field reverses in the  $-E$  hemisphere, and suggested that the field lines wrap the planet more tightly on the nightside  $-E$  hemisphere than on the  $+E$  hemisphere. On the other hand, a global looping magnetic field around the Venusian magnetotail has been proposed by Vaisberg & Smirnov (1980)

based on the observations of Venera-10. Many years later, based on the observations of the Pioneer Venus Orbiter (PVO; Russell 1992), Verigin et al. (1993) independently proposed the looping structure. In order to investigate the magnetic anomalies observed by VEX, Chai et al. (2016) statistically examined the magnetic field data observed by VEX, PVO, and Messenger and independently found the looping structure and provided detailed characterization of the looping field. The main difference between the  $E$ -asymmetry structure and the looping structure is their magnetic morphologies. The  $E$ -asymmetry structure focuses only on the magnetic field component antiparallel to the transverse IMF,  $B_y$  (Figure 4 in Zhang et al. 2010), while the looping structure focuses on both the antiparallel and perpendicular components,  $B_y$  and  $B_z$  (Figure 8 in Chai et al. 2016 and Figure 5 in Verigin et al. 1993). It is worth noting that the three-dimensional magnetic morphologies constructed by Chai et al. (2016) and Verigin et al. (1993) are also different. The different magnetic morphologies imply different understandings of the formation mechanism of abnormal magnetic fields.

Considering the similarities shared by Mars and Venus in their interactions with the solar wind, Mars is a promising candidate to study the abnormal magnetic field that are inconsistent with draped IMF and crustal fields. Mars and Venus share similarities but also differ in many aspects (Luhmann et al. 1991). Mars has a smaller gravity, a weaker atmosphere, a larger Sun-planet distance, stronger crustal fields, and therefore a more extended exosphere, a weaker ionosphere, and a more complex magnetosphere. The solar wind around Mars has a smaller dynamic pressure, a lower density, and a weaker IMF than that around Venus (Slavin & Holzer 1981). In this Letter, we investigate the global looping magnetic field on Mars and its similarities to and differences from that on Venus. We first show the observations of the global looping magnetic field on Mars with the MAVEN data and the comparison of the looping fields between Mars and Venus; then, we analyze its formation mechanism.

## 2. Data

In 2014 September, MAVEN started orbiting Mars with an orbital period of 4.5 hr (Jakosky et al. 2015) and completed 3660 orbits by 2015 August. The MAVEN data collected during this time period are used to conduct statistical analysis. To understand the magnetic field morphology and the solar wind motion around Mars, the 1 s data of the Magnetometer (MAG; Connerney et al. 2015) and the 8 s data of the Solar Wind Ion Analyzer (SWIA; Halekas et al. 2015) are analyzed. The 4 s data of the VEX magnetometer (Zhang et al. 2006) observed on Venus in 3138 orbits from 2006 April to 2014 December are also employed for comparison.

The statistical analysis is conducted in both Mars-solar-orbital (MSO) and Mars-solar-electrical (MSE) coordinate systems. In the MSO system,  $X$  points from Mars toward the Sun,  $Y$  is antiparallel to the planetary orbital motion, and  $Z$  completes the orthogonal coordinate set. In the MSE system,  $X$  points from Mars against the solar wind velocity,  $v_{\text{SW}}$ , with an average  $3.8^\circ$  aberration removed,  $Z$  parallels the conventional electric field,  $\mathbf{E} = -v_{\text{SW}} \times \mathbf{B}$ , and  $Y$  completes the orthogonal coordinate set, where  $\mathbf{B}$  is the IMF. For statistical analyses in the MSE frame, we consider only orbits with relatively steady IMF directions. The selection criterion is that the IMF observed after the outbound bow shock crossing is rotated by less than  $90^\circ$  from the IMF observed before the inbound bow shock

crossing. To describe the looping field structure, cylindrical coordinates  $(\chi, \rho, \phi)$  are introduced in both MSO and MSE frames, where  $\chi$  is antiparallel to the  $X$  axis,  $\rho$  is the radial distance from  $\chi$ , and  $\phi$  is the azimuthal angle measured counterclockwise from the  $Y$  axis looking from the tail toward the planet.

## 3. Results

Figure 1 presents two examples of the looping magnetic fields observed on Mars by MAVEN on 2015 March 10 and December 30. The red rectangles in panels (a, c) and the corresponding red arrows in panels (b, d) highlight the magnetic fields consistent with the global looping field structure seen on Venus (Chai et al. 2016). In the first case, most of the orbit is in the magnetotail region, where the large-scale looping fields can be observed. As shown in Figure 1(a), a positive  $B_y$  (inside the red rectangle) is observed around the northern region of the magnetotail, while  $B_y$  in the magnetosheath remains negative. The scale of the positive  $B_y$  reaches at least  $2.2 R_M$  (where  $R_M = 3389.5$  km is the Mars radius) from point  $(x = -0.30R_M, y = 0.74R_M, z = 0.81R_M, \text{altitude} = 475 \text{ km})$  at 10:39 UT to point  $(x = -1.64R_M, y = -1.03R_M, z = 0.72R_M, \text{altitude} = 3635 \text{ km})$  at 11:22 UT. On this path, the crustal magnetic field strength inferred from the Cain model (Cain et al. 2003) is negligible. The  $B_y$  in the magnetosheath becomes negative at 3:00 UT in the previous orbit (not shown; the previous orbital  $B_y$  is generally the same as this one). It can be presumed that the IMF  $B_y$  has remained negative for approximately 7 hr before the large-scale positive  $B_y$  is observed, and therefore, the large-scale positive  $B_y$  is unlikely to be a fossil field of the IMF (Luhmann et al. 1984). In conclusion, the observed large-scale positive  $B_y$  is not a draped IMF, a crustal field, or an IMF fossil field. Furthermore, as shown in Figure 1(b), the direction and location of the large-scale positive  $B_y$  (red arrows) are consistent with the structure of the global looping magnetic field seen on Venus (shown by the red triangle and the red circle). In the second case, the orbit is approximately parallel to the terminator. A looping field observation is presented when the IMF  $B_y$  is positive. As shown in Figure 1(c), a large-scale negative  $B_y$  (inside the red rectangle) is observed around the southern region of the magnetotail, while the  $B_y$  in the solar wind and magnetosheath remain positive. The crustal field there is negligible. Thus, the large-scale negative  $B_y$  is not a draped IMF or a crustal field. Furthermore, the direction and location of the large-scale negative  $B_y$  are consistent with the structure of the global looping magnetic field seen on Venus (Figure 1(d)). From these two cases, it can be seen that the explanation of the Martian magnetic field may have something in common with the explanation of the Venusian magnetic field.

Figure 2 shows the global distributions of the looping magnetic fields on Mars and Venus for comparison. The average values of the magnetic field magnitude  $|\mathbf{B}|$ , the magnetic field azimuthal component  $B_\phi$ , and the azimuthal component direction  $\text{sign}(B_\phi)$  are calculated in the bins  $0.1R_p \times 0.1R_p$  ( $R_p$  is the planetary radius) on the  $\chi\rho$  planes in the MSO and Venus-solar-orbiter (VSO; equivalent to MSO on Mars) coordinate systems, respectively. The nightside average  $B_\phi$  is calculated along the negative  $X$ -axes and projected on the  $YZ$  planes. The distribution of  $|\mathbf{B}|$  is a good indicator of the locations of planetary bow shocks and magnetotails. As shown in Figures 2(a), (e), the outer

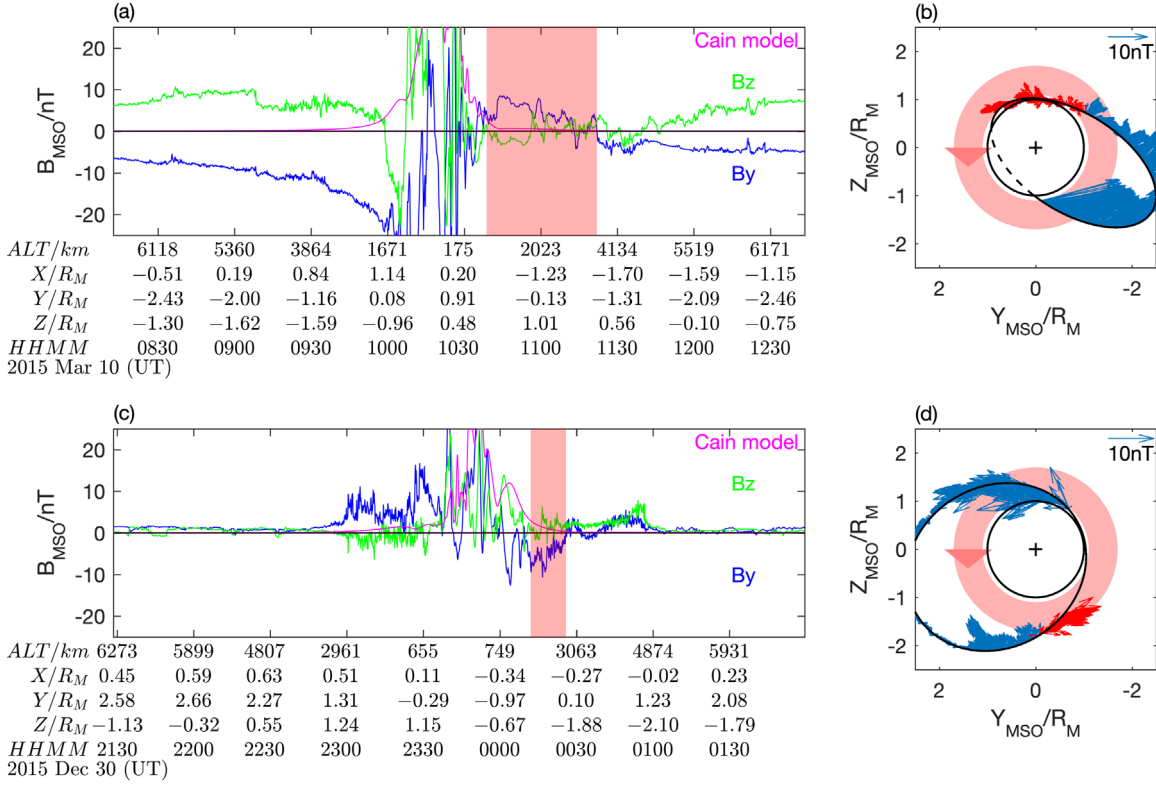


**Figure 1.** Magnetic field observations by MAVEN in two orbits on March 10 (a-b) and December 30 (c-d) in 2015 in the MSO coordinate system. (a, c) are the time series plots of the transverse magnetic field components,  $B_y$  (blue) and  $B_z$  (green), and the expected crustal field magnitude,  $|B_{\text{cain}}|$  (magenta; Cain et al. 2003). The red rectangles highlight the magnetic fields consistent with the global looping magnetic field but not with draped IMFs or crustal fields. (b, d) are the vectors of the magnetic field with a weak crustal field ( $|B_{\text{cain}}| < 3\text{nT}$ ) projected onto the terminator as viewed from the tail. The black circles represent the planetary surface. The red hollow circles and triangles represent the locations and directions of the global looping field. The red arrows represent the projection of the magnetic field vectors inside the red rectangles in (a, c).

boundaries of the enhanced  $|B|$  coincide very well with the bow shock models on Mars (Edberg et al. 2008) and Venus (Chai et al. 2014). The strong magnetic fields on the nightsides of the planets indicate that the magnetotails on Mars and Venus have radii of approximately  $1.7 R_M$  and  $1.3 R_V$  (black rectangles), respectively, and average magnetic magnitudes of  $9.4 \text{ nT}$  and  $12.1 \text{ nT}$ , respectively. Here, the average IMF magnitudes around Mars and Venus are  $4.0 \text{ nT}$  and  $10.2 \text{ nT}$ , respectively. The ratio of the magnetic field of the Martian magnetotail to the IMF upstream of the bow shock is 2.25, which agrees with the Phobos-2 observations (Yeroshenko et al. 1990). As shown in Figure 2(b), the looping field  $B_\phi$  on Mars is dominantly positive in the region just inside the outer boundary of the magnetotail, similar to that on Venus (Figure 2(f)). The distribution thicknesses of the looping fields (positive  $B_\phi$  in the black rectangles in Figures 2(b), (f)) are  $1.1 R_M$  from  $0.6$  to  $1.7 R_M$  on Mars and  $0.6 R_V$  from  $0.7$  to  $1.3 R_V$  on Venus. The magnitudes of the looping field on Mars and Venus are  $1.8 \text{ nT}$  and  $1.1 \text{ nT}$  on average,  $2.5 \text{ nT}$  and  $1.6 \text{ nT}$  at  $x = -1R_p$ , and  $1.9 \text{ nT}$  and  $1.0 \text{ nT}$  at  $x = -2R_p$ , respectively. Although the strength of the looping fields on both planets decreases with distance from the planets, the counterclockwise direction of the looping fields (positive  $\text{sign}(B_\phi)$  in the black rectangles in Figures 2(c), (g)) remains unchanged even in the far-tail region. The occurrence probabilities  $p$  of the looping magnetic fields are 70.9% on Mars and 63.4% on Venus, as calculated with  $p = (\langle \text{sign}(B_\phi) \rangle + 1)/2$ , where  $\langle \text{sign}(B_\phi) \rangle$  is the average direction in the black rectangles in Figures 2(c), (g). As shown in Figure 2(d), the looping field on Mars distributes evenly all

around the magnetotail in the MSO coordinate system, similar to that on Venus (Figure 2(h)). The statistical analysis on Mars and Venus proves that the main characteristics of the looping fields on Mars and Venus are the same, but on Mars, the looping field has a larger magnitude, higher occurrence probability and more dispersive distribution relative to the planetary radius.

Figure 3 shows the magnetic field and the solar wind transverse velocity on the nightside of Mars in the MSE coordinate system, in which the transverse IMF always points in the  $+Y$  direction. The average magnitudes and directions of the magnetic field components ( $B_x$ ,  $B_y$ ,  $B_z$ ,  $B_\phi$ ) and the solar wind velocity components ( $V_\rho$ ,  $V_\phi$ ) are calculated along the negative  $X$ -axis and projected on the  $YZ$  plane. The classical magnetic draping structure consists of  $-/+B_x$  in the  $+/-Y_{\text{MSE}}$  lobes of the magnetotail (Figures 3(a), (e)). In the magnetosheath region ( $\rho > 1.7R_M$ , outside the outer black circles), all  $B_y$  are positive or parallel to the IMF (Figures 3(b), (f)), and the  $B_z$  distribute in a quadrupole pattern, i.e.,  $-/+B_z$  in  $+/- (Y_{\text{MSE}} \cdot Z_{\text{MSE}})$  region (Figures 3(c), (g)), which is also seen on Venus (Rong et al. 2014). In the looping field region ( $0.6 < \rho < 1.7R_M$ , near the inside of the outer black circles), both  $B_y$  and  $B_z$  are distributed in a dipole pattern, i.e.,  $+/-B_y$  in the  $+/-Z_{\text{MSE}}$  region and  $-/+B_z$  in the  $+/-Y_{\text{MSE}}$  region (black arrows), which constitutes a global looping magnetic field. As shown in Figures 3(d), (h), the azimuthal magnetic field  $B_\phi$  is positive or counterclockwise (black arrows) all around the magnetotail region. Statistical analysis in the MSE coordinate system proves the existence of the global looping magnetic field when the transverse direction of the IMF is

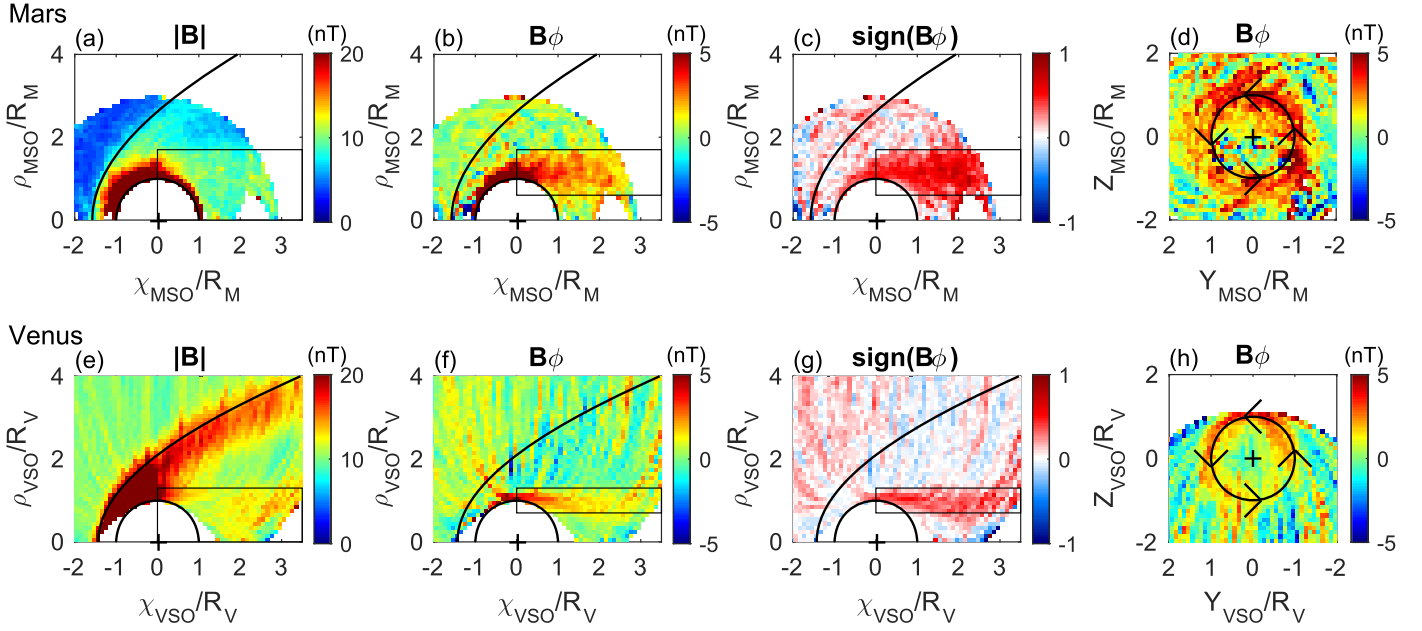


**Figure 2.** Comparison of the global looping magnetic fields on Mars (a-d) and Venus (e-h) in the MSO and VSO coordinate systems, respectively. (a, e), (b, f), and (c, g) are, respectively, the distributions of the average magnetic field magnitudes,  $|\mathbf{B}|$ , magnetic field azimuthal components,  $B_\phi$ , and azimuthal magnetic field directions,  $\text{sign}(B_\phi)$ , on the  $\chi\rho$  plane. (d, h) are the distribution of the nightside average  $B_\phi$  on the YZ plane (terminator), as viewed from the tail toward the planet averaged along the  $\chi$ -axis. The black semicircles in (a-c, e-g) and the black circles in (d, h) represent the planetary surfaces. The black curves in (a-c, e-g) represent the bow shock locations. The black rectangles in (a, e) represent the locations of the magnetotails, and those in (b-c, f-g) represent the locations of the looping magnetic fields. The black arrows in (d, h) indicate the  $+\phi$  direction.

stable. The statistical analysis also shows that the fields from the two cases studied in Figure 1 occur often enough that they dominate the statistical picture of magnetic fields on Mars.

As shown in Figures 3(i), (k), the solar wind plasma moves away from the Sun-planet line with an average velocity of  $V_\rho = 55 \text{ km s}^{-1}$  in the magnetosheath region and toward the Sun-planet line at an average velocity of  $V_\rho = -9 \text{ km s}^{-1}$  in the magnetotail region ( $\rho < 1.7R_M$ , inside the outer black circles). The  $V_\rho$  near the current sheet ( $Y = 0$ ) in the magnetosheath is larger in the  $-E$  ( $-Z_{\text{MSE}}$ ) hemisphere than in the  $+E$  hemisphere. This result is consistent with Dubinin et al. (2018), i.e., the solar wind plasma is deflected toward  $-E$  direction in the magnetosheath region. As shown in Figures 3(j), (l), the solar wind plasma in the vicinity of the outer boundary of the magnetotail ( $\rho \sim 1.7R_M$ , near the outer black circles) moves in a counterclockwise/clockwise ( $+/-V_\phi$ ) direction (black arrows) in the  $+/-Y_{\text{MSE}}$  hemisphere with a magnitude of about  $|V_\phi| = 14 \text{ km s}^{-1}$ . In other words, the solar wind plasma in the two magnetotail lobes moves toward the  $-E$  ( $-Z_{\text{MSE}}$ ) hemisphere and then in the  $-E$  ( $-Z_{\text{MSE}}$ ) hemisphere they move toward the center of the current sheet ( $Y_{\text{MSE}} = 0$ ) and converge with each other over the  $-E$  magnetotail polar region ( $X_{\text{MSE}} < 0$ ,  $Y_{\text{MSE}} = 0$ ,  $Z_{\text{MSE}} < -1R_M$ ). The magnetic field structure should be modified by  $V_\rho$  in the magnetosheath region, where  $|V_\rho| \gg |V_\phi|$  and by  $V_\phi$ , and  $V_\rho$  in the looping field region, where  $|V_\phi| \gtrsim |V_\rho|$ . The ratio of azimuthal velocity to axial velocity ( $|V_\phi/V_x| \approx 14\%$ ) approximates to the ratio of looping field to draped field ( $|B_\phi/B_x| \approx 20\%$ ); here, the solar wind axial velocity  $|V_x|$  is approximately  $100 \text{ km s}^{-1}$  in the magnetotail. Thus, the observed azimuthal flow toward the  $-E$  magnetotail polar region can be a possible cause of the global looping magnetic field.

Figure 4 illustrates step by step how a counterclockwise looping magnetic field can be formed by the observed solar wind azimuthal flows toward the  $-E$  magnetotail polar region. First, the draping of an IMF in the  $+Y$  direction forms a  $+/-B_x$  (sunward/anti-sunward) in the  $-/+Y$  magnetotail lobe (Figure 4(a)). Here, the current sheet is usually thicker in the  $+E$  hemisphere than in the  $-E$  hemisphere (Zhang et al. 2010). Then the solar wind azimuthal flows bend the field lines in both lobes toward the  $-E$  ( $-Z$ ) direction, forming a  $+/-B_z$  in the  $-/+Y$  lobe, and bend the field lines in the  $-E$  ( $-Z$ ) hemisphere toward the current sheet center ( $Y = 0$ ), forming a  $-B_y$  in the  $-Z$  hemisphere (Figure 4(b)). Together with the draped IMF in the  $+E$  hemisphere ( $+B_y$  in the  $+Z$  hemisphere), a counterclockwise magnetic field (viewed from the tail) is formed around most of the circumference of the magnetotail. A closed looping magnetic field can be formed by magnetic reconnection (Figure 4(c)). It should be noted that magnetic reconnection is not necessary to form the observed looping magnetic field features. With one-point observations, it is hard to confirm whether or not the looping magnetic field is closed. Figures 4(d)–(f) illustrate how the same counterclockwise looping magnetic field is formed when the IMF is in the opposite direction ( $-Y$ ). Corresponding to the inverse IMF direction (Figure 4(d)), both the draped magnetic field direction ( $-/+B_x$  in  $-/+Y$  lobe) and the solar wind  $E$  direction ( $-Z$ ) reverse. It is the double reverse that keeps the looping field direction unchanged. As shown in Figure 4(e), the solar wind azimuthal flows bend the draped field lines (in the reverse direction) toward  $-E$  ( $+Z$ ) magnetotail polar region (position reversed). Now the same  $+/-B_z$  in the  $-/+Y$  lobe and the same  $+B_y$  in the  $+Z$  hemisphere are formed. Together with the draped IMF ( $-B_y$ ) in the  $-Z$  hemisphere, the same counterclockwise looping magnetic field is formed. In conclusion, no matter what direction the IMF is pointing in (Figures 4(a), (d)), a counterclockwise looping magnetic field can be formed by



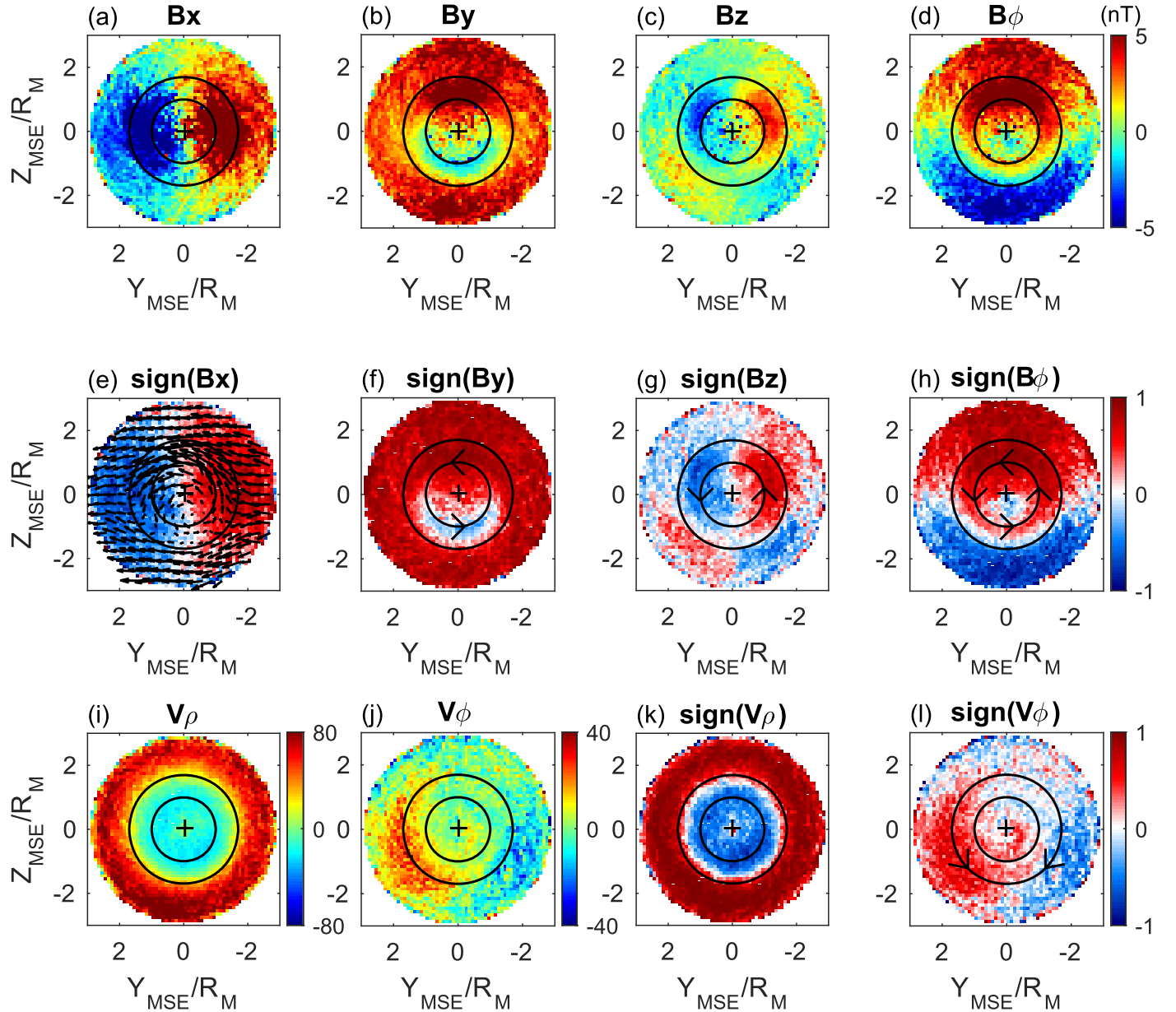


**Figure 3.** Magnetic field structure and the solar wind transverse velocity observed on the nightside of Mars in the MSE coordinate system. (a-h) are the distributions of the average magnitudes (a-d) and directions (e-h) of the magnetic field components  $B_x$ ,  $B_y$ ,  $B_z$ , and  $B_\phi$  on the  $YZ$  plane, as viewed from the tail toward the planet. (i-l) are the distributions of the average magnitudes (i-j) and directions (k-l) of the solar wind radial velocity  $V_\rho$  and azimuthal velocity  $V_\phi$ . The black arrows in (e) represent the  $B_y$  and  $B_z$  field vectors. The inner and outer black circles represent the planetary surface ( $\rho = 1R_M$ ) and the outer boundary of the magnetotail ( $\rho = 1.7R_M$ ), respectively. The black arrows in (f-h) indicate the local magnetic field directions, and these in (l) indicate the local azimuthal velocity directions.

the observed azimuthal flows toward the  $-E$  magnetotail polar region (Figures 4(b), (e)).

#### 4. Summary and Discussion

In this Letter we conducted both case studies and statistical analysis of MAVEN data to investigate whether or not the global looping magnetic field seen on Venus also exists on Mars and how it forms. The direct observations of the magnetic fields that can be identified as parts of the global looping magnetic field are presented in the two case studies (Figure 1). The statistical study of the magnetic fields on Mars (Figure 2) proves that the global looping magnetic field ( $+B_\phi$ ) also exists on Mars. Therefore, the global looping magnetic field is a common feature of unmagnetized planetary bodies with

ionospheres and should exist on Titan and near-Sun comets as well. Some of the magnetic fields observed at Titan (e.g., Figure 6 in Ness et al. 1982, and Figure 3 T30 in Bertucci et al. 2008) and Comet 67P/C-G (e.g., Figure 2 in Koenders et al. 2016) are consistent with the global looping field structure.

Figure 5 is a summary illustration of the formation process of the global looping magnetic field in the MSE coordinate system. When the high-speed solar wind plasma encounters the planetary oxygen ions, the planetary oxygen ions are accelerated by the solar wind conventional  $E$  and form a strong oxygen plume along the  $+E$  direction (thick red curved arrow; Dong et al. 2015). Due to the conservation of momentum, acceleration of the planetary ions causes the solar wind to accelerate in the opposite direction ( $-E$ ; e.g., Dubinin et al. 2018). Based on these observations and studies, we

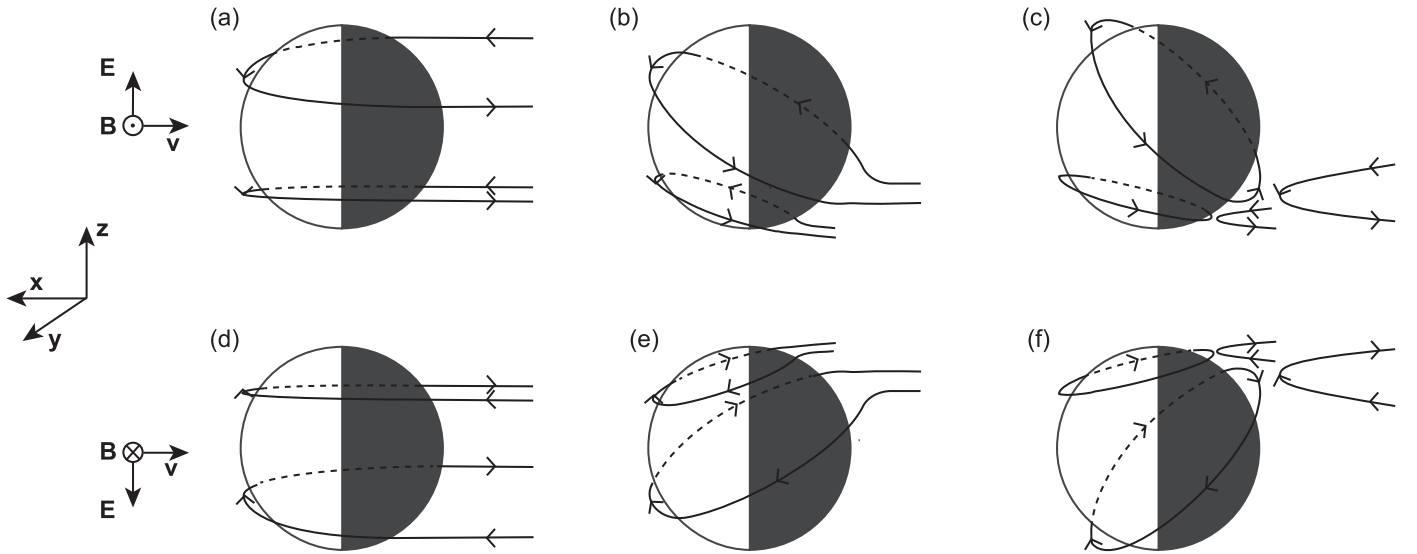


**Figure 4.** Step-by-step schematic illustrations of the formation of counterclockwise (view from tail) looping magnetic fields by solar wind azimuthal flows toward the  $-E$  magnetotail polar region under opposite IMF conditions, (a-c) for an IMF pointing out of the page and (d-f) for an IMF pointing in. The black curves show the magnetic field lines with arrows indicating their directions. The dashed curves show the field lines behind the planet.

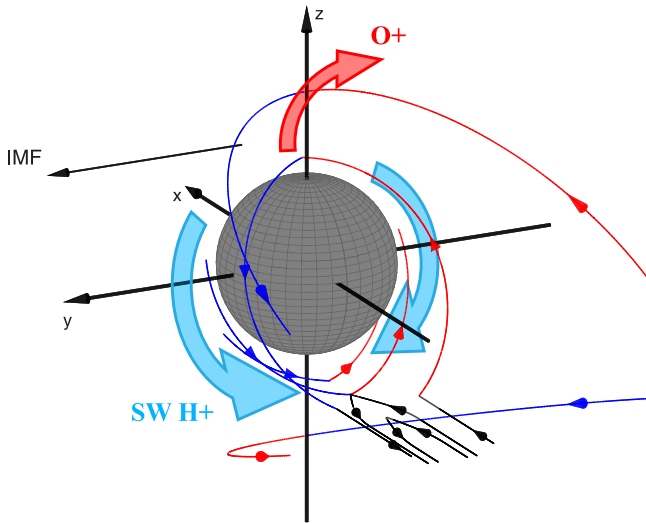


**Figure 5.** Summary illustration of the magnetic field morphology and the plasma flow patterns observed on Mars. The thick red curved arrow shows the planetary  $O^+$  plume observed in Dong et al. (2015). The thick blue curved arrows show the solar wind azimuthal flows observed in Figure 3(l). The curves show the magnetic field lines constructed from Figures 3(e)–(h) with arrows indicating their directions. The thin curve color (red/black/blue) indicates the  $sign(B_z)$  (+/0/-) in Figure 3(g).

propose that when the solar wind plasma moves toward the  $-E$  hemisphere, the magnetotail will act as a block and force the solar wind plasma to move azimuthally around it. Then, the solar wind plasma will obtain the observed counterclockwise/clockwise velocity in the  $+/-Y_{MSE}$  hemisphere in Figure 3(l) (thick blue curved arrows). These solar wind azimuthal flows drag the draped magnetic field lines (colored thin curves) together with them and bend the field lines toward the  $-E$  magnetotail polar region. Then, the observed counterclockwise looping magnetic field in Figure 3(h) is formed. Because field lines with opposite directions are pushed toward each other over the  $-E$  magnetotail polar region, more magnetic reconnection (crossed curves) can be expected there, and closed looping magnetic fields can be formed. This scenario

also explains why more magnetic reconnection is observed in the  $-E$  hemisphere than in the  $+E$  hemisphere in the Martian magnetotail (Harada et al. 2017). Based on these propositions, the magnitude of the looping field should correlate with the  $E$  asymmetry effect (Cloutier et al. 1974; Dong et al. 2015). The  $E$  asymmetry is caused by the finite gyroradius effect of ions, i.e., the  $E$  accelerates ions and electrons in opposite directions by  $F = qE$ ; because the gyroradius of ions is much larger than that of electrons, ions carry most of the momentum of plasma. The direction of the looping field, counterclockwise, should be determined by the mass asymmetry of the plasma; i.e., the heavy ions carry a positive charge, and the light electrons carry a negative charge. The stronger oxygen plume and more extended exosphere might be the reason why Mars has a stronger looping field than Venus (Figures 2(b), (f)). The ion gyroradius, the exosphere, and the dynamic pressure could all affect the spatial distribution of the looping field at Mars (Figures 2(c), (g)). With the accumulating data of MAVEN, the detailed characteristics of looping fields can be investigated in future research.

The current system associated with the looping magnetic field is mainly field-aligned currents at its inner and outer boundaries. The inner ones flow tailward from the ionosphere to the far-tail region, and the outer ones flow sunward from the far-tail region to dayside (see Figure 6 in Chai et al. 2016). The looping field currents along the magnetotail are physically more like the Birkeland currents in the polar region on magnetized planets (Iijima & Potemra 1976) than the currents in magnetotails, which are usually perpendicular to the magnetic field (Baumjohann et al. 2010; Fatemi et al. 2013). The intensity of the looping field current,  $I_{loop}$ , is approximately  $3.5 \times 10^4 A$  on Mars, as calculated with  $I_{loop} = 2\pi r B_\phi / \mu_0$  for an average looping field magnitude  $B_\phi = 1.8 nT$  and radius  $r = 1.15 R_{Mars}$ . It is worth noting that the  $B_\phi$  is larger near the planet (Figure 2(b)) and in some cases can be as large as 10 nT (Figure 1), therefore  $I_{loop}$  can be as large as  $2 \times 10^5 A$ . Thus, the looping field currents on Mars are approximately one magnitude smaller than Birkeland currents on Earth (Iijima et al. 1984). The electron precipitation from the magnetotails into planetary atmospheres is the

main source of the nightside ionospheres on Mars and Venus (Gringauz et al. 1979; Verigin et al. 1991; Fowler et al. 2015). The tailward ion escape is the main channel of planetary ion escapes, constituting approximately 77% of the total escape on Mars (Dong et al. 2015). Considering the fact that the Birkeland currents are directly associated with the aurora and electron accelerations on Earth (Potemra 1988; Newell et al. 1996), the inner currents of the looping fields that flow tailward from the ionospheres may influence the ionospheres and atmospheres on Mars and Venus, especially as their tailward direction favors enhancement of the fluxes of precipitating electrons from the magnetotail and tailward escaping ions.

The discoveries of global looping magnetic fields on both Mars and Venus have shed new light on the global morphology of induced magnetospheres, as well as nightside ionosphere formations and planetary ion escapes. However, many questions remain for future studies, such as the looping field characteristics, the looping field in the dayside ionosphere, and the closure of the looping field currents. It will also be very interesting to study the relationship between the looping field currents and the nightside ionosphere formations and planetary ion escapes on Mars and Venus.

We thanks R. J. Strangeway, C. T. Russell, and M. G. Kivelson at UCLA and M. I. Verigin at IKI for valuable discussions and suggestions. We thank the MAVEN and VEX teams for providing data. This work was supported by the National Science Foundation of China (41621063, 41674177, 41874208, 41404138, 41525016, 41474155). The MAVEN data are available at <https://lasp.colorado.edu/maven/sdc/public/>. The VEX data are available at <https://www.cosmos.esa.int/web/psa/Venus-express>.

### ORCID iDs

Lihui Chai  <https://orcid.org/0000-0001-8844-9176>

Jun Zhong  <https://orcid.org/0000-0003-4187-3361>

### References

Acuna, M. H., Connerney, J. E. P., Ness, N. F., et al. 1999, *Sci.*, **284**, 790  
 Acuna, M. H., Connerney, J. E. P., Wasilewski, P., et al. 1998, *Sci.*, **279**, 1676  
 Baumjohann, W., Blanc, M., Fedorov, A., & Glassmeier, K.-H. 2010, *SSRv*, **152**, 99  
 Bertucci, C., Achilleos, N., Dougherty, M. K., et al. 2008, *Sci.*, **321**, 1475

Brain, D. A., Bagenal, F., Acuna, M. H., & Connerney, J. E. P. 2003, *JGRA*, **108**, 1424  
 Cain, J. C., Ferguson, B. B., & Mozzoni, D. 2003, *JGRE*, **108**, 5008  
 Chai, L., Fraenz, M., Wan, W., et al. 2014, *JGRA*, **119**, 9464  
 Chai, L., Wei, Y., Wan, W., et al. 2016, *JGRA*, **121**, 688  
 Cloutier, P. A., Daniell, R. E., & Butler, D. M. 1974, *P&SS*, **22**, 967  
 Connerney, J. E. P., Acuna, M. H., Wasilewski, P. J., et al. 1999, *Sci.*, **284**, 794  
 Connerney, J. E. P., Espley, J., Lawton, P., et al. 2015, *SSRv*, **195**, 257  
 DiBraccio, G. A. 2018, *GeoRL*, **45**, 4559  
 Dolginov, S. S. 1987, *EM&P*, **37**, 17  
 Dong, Y., Fang, X., Brain, D. A., et al. 2015, *GeoRL*, **42**, 8942  
 Dubinin, E., Fraenz, M., Pätzold, M., et al. 2018, *GeoRL*, **45**, 2574  
 Dubinin, E., Fraenz, M., Zhang, T. L., Woch, J., & Wei, Y. 2014a, *GeoRL*, **41**, 6329  
 Dubinin, E., Fraenz, M., Zhang, T. L., Woch, J., & Wei, Y. 2014b, *JGRA*, **119**, 7587  
 Edberg, N. J. T., Lester, M., Cowley, S. W. H., & Eriksson, A. I. 2008, *JGRA*, **113**, A08206  
 Fatemi, S., Holmstrom, M., Futaana, Y., Barabash, S., & Lue, C. 2013, *GeoRL*, **40**, 17  
 Fowler, C. M., Andersson, L., Ergun, R. E., et al. 2015, *GeoRL*, **42**, 8854  
 Gringauz, K. I., Verigin, M. I., Breus, T. K., & Gombosi, T. 1979, *JGRA*, **84**, 2123  
 Halekas, J. S., Taylor, E. R., Dalton, G., et al. 2015, *SSRv*, **195**, 125  
 Harada, Y., Halekas, J. S., McFadden, J. P., et al. 2015a, *GeoRL*, **42**, 8925  
 Harada, Y., Halekas, J. S., McFadden, J. P., et al. 2017, *JGRA*, **122**, 5114  
 Iijima, T., & Potemra, T. A. 1976, *JGR*, **81**, 5971  
 Iijima, T., Potemra, T. A., Zanetti, L. J., & Bythrow, P. F. 1984, *JGRA*, **89**, 7441  
 Jakosky, B. M., Lin, R. P., Grebowsky, J. M., et al. 2015, *SSRv*, **195**, 3  
 Koenders, C., Goetz, C., Richter, I., Motschmann, U., & Glassmeier, K.-H. 2016, *MNRAS*, **462**, S235  
 Luhmann, J. G., Dong, C., Ma, Y., et al. 2015, *GeoRL*, **42**, 9087  
 Luhmann, J. G., Russell, C. T., & Elphic, R. C. 1984, *JGRA*, **89**, 362  
 Luhmann, J. G., Russell, C. T., Schwingenschuh, K., & Yeroshenko, Y. 1991, *JGRA*, **96**, 11199  
 Mohlmann, D. 1992, *AdSR*, **12**, 213  
 Ness, N. F., Acuna, M. H., Behannon, K. W., & Neubauer, F. M. 1982, *JGRA*, **87**, 1369  
 Newell, P. T., Lyons, K. M., & Meng, C.-I. 1996, *JGRA*, **101**, 2599  
 Potemra, T. A. 1988, *Ap&SS*, **144**, 155  
 Riedler, W., Mohlmann, D., Oraevsky, V. N., et al. 1989, *Natur*, **341**, 604  
 Rong, Z. J., Barabash, S., Futaana, Y., et al. 2014, *JGRA*, **119**, 8838  
 Russell, C. T. 1992, *GMS*, **66**, 225  
 Russell, C. T., Elphic, R. C., & Slavin, J. A. 1979, *Sci.*, **205**, 114  
 Saunders, M. A., & Russell, C. T. 1986, *JGRA*, **91**, 5589  
 Slavin, J. A., & Holzer, R. E. 1981, *JGRA*, **86**, 11401  
 Vaisberg, O. L., & Smirnov, V. N. 1980, *KosIs*, **18**, 651  
 Verigin, M., Luhmann, J. G., & Russell, C. T. 1993, in *COSPAR Coll. 4, Plasma Environments of Non-Magnetic Planets*, ed. T. I. Gombosi, **259**  
 Verigin, M. I., Gringauz, K. I., Shutte, N. M., et al. 1991, *JGRA*, **96**, 19307  
 Yeroshenko, Y., Riedler, W., Schwingenschuh, K., et al. 1990, *GeoRL*, **17**, 885  
 Zhang, T. L., Baumjohann, W., Delva, M., et al. 2006, *P&SS*, **54**, 1336  
 Zhang, T. L., Baumjohann, W., Du, J., et al. 2010, *GeoRL*, **37**, L14202